

Experimental Study of Interfacial Shear Stresses in FRP-Strengthened RC Beams

Stephen Kurtz, P.E., A.M.ASCE¹; Perumalsamy Balaguru, M.ASCE²; and Jeffrey Helm³

Abstract: This paper presents the results of an experimental study on the distribution of shear stresses along the interface between concrete and the carbon fiber-reinforced polymer (FRP) in 29 plate-strengthened beams, where the primary test variables are: Clear cover, plate length, plate thickness (area), and compressive strength of concrete. FRP strain measurement was accomplished using either the photographic technique of digital image correlation or a series of electrical-resistance strain gages, both providing similar results. The distribution of shear stresses is found to be smoother than predicted by several analytical expressions available in the literature. Another substantial observation is the existence of a second region of peak stress, occurring near the center of the shear span in all of the beams with longer plate lengths, which the authors believe is associated with the singular application of shear corresponding to the point load, as well as the transition from elastic to plastic behavior occurring in the rebar. Because the overall nature of the stress distribution is sufficiently smooth, it is very reasonable to approximate it as a constant stress.

DOI: 10.1061/(ASCE)1090-0268(2008)12:3(312)

CE Database subject headings: Concrete, reinforced; Concrete beams; Fiber reinforced polymers; Digital techniques; Shear stress.

Introduction

Since 1991, considerable research has been conducted on the strengthening of existing reinforced concrete beams by the external bonding of fiber-reinforced polymer (FRP) plates (Saadatmanesh and Ehsani 1991; Ritchie et al. 1991). However, as described by Colotti et al. (2004), the problem of predicting the failure modes is far from being solved, in particular, the problem of predicting plate debonding. This failure mode, characterized by a sudden rupture of the concrete at its interface with the bonded plate, has been observed by many researchers using FRP plates (Saadatmanesh and Ehsani 1991; Ritchie et al. 1991; Quantrill et al. 1996; Sharif et al. 1994; Spadea et al. 1998), as well as steel plates (Jones et al. 1988; Oehlers 1992). Typically, the bond between concrete and the reinforcing plate remains intact, as evidenced by a firm bond remaining between the adhesive and the concrete aggregate, while the bond within the concrete matrix is destroyed, resulting either in a distinct failure surface at the rebar level or the disintegration of the concrete into aggregate-sized particles.

In general, the problem of predicting a failure event requires two kinds of knowledge. The first is a failure theory with a mathematical description of the stress-strain conditions that result in

failure. The second kind of knowledge, the subject of this paper, is a description of how stresses and strains are distributed within the failure region. In this particular case, the focus is on the distribution of shear stresses along the entire FRP-concrete interface.

The distribution of interfacial shear stress has received considerable attention, particularly from analytical researchers (Roberts and Haji-Kazemi 1989; Roberts 1989; Arduini and Di Leo 1996; Täljsten 1997; Malek et al. 1998; Shen et al. 2001). In these cases, researchers have contributed to the study of debonding failure by assuming linear behavior and that failure initiation is due to concentration of shear and normal (peeling) stresses at the end of the plate.

One of the most often cited analytical works is by Roberts (1989), based on his comparisons with the work of Jones et al. (1988), suggested that plate debonding failure occurs when shear stress between 3 and 5 MPa is combined with normal stress between 1 and 2 MPa. However, as determined by Mukhopadhyaya and Swamy (2001), Roberts' approach yields a very wide scatter of peak shear and normal stresses at failure, when the predictive equations are used on experimental beams from the literature. This suggests that focusing on plate-end stresses, using linear-elastic assumptions, may not be a reliable means of predicting failure. Similarly, other analytical predictions in the literature, though yielding less extreme peak values, employ the same assumption of linear elastic material properties, leading to severe concentrations in shear and normal stress at the plate end.

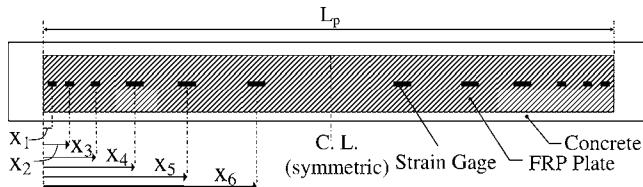
In significant contrast, Mukhopadhyaya and Swamy (2001) question the validity of the plate-end stress concentration basis for failure entirely, suggesting instead that a much more consistent method of predicting debonding failure is based on the easily computed uniform elastic shear stresses. At the same time, they point out the need for experimental evidence to confirm or contradict the existence of plate-end stress concentrations. Hence, the purpose of this research paper is to present experimental results for the shear stress distribution over the entire plate length, but particularly at its termination.

¹Assistant Professor, Dept. of Civil and Environmental Engineering, Lafayette College, Easton, PA 18042.

²Program Director, Infrastructure Materials and Structural Mechanics, National Science Foundation, Arlington, VA 22203.

³Assistant Professor, Dept. of Mechanical Engineering, Lafayette College, Easton, PA 18042.

Note. Discussion open until November 1, 2008. Separate discussions must be submitted for individual papers. To extend the closing date by one month, a written request must be filed with the ASCE Managing Editor. The manuscript for this paper was submitted for review and possible publication on June 22, 2006; approved on August 24, 2006. This paper is part of the *Journal of Composites for Construction*, Vol. 12, No. 3, June 1, 2008. ©ASCE, ISSN 1090-0268/2008/3-312-322/\$25.00.



L_p (mm)	Distances (mm)					
	x_1	x_2	x_3	x_4	x_5	x_6
1720	32	100	170	292	465	725
2235	32	100	255	475	725	980

Fig. 1. Strain gage locations along FRP plate; view from underneath

Experimental Program

The objective of the experimental program was to study the distribution of interfacial shear stresses along the entire length of a carbon FRP plate bonded to the tension side of a precracked reinforced concrete beam. The intention was to pay particular attention to behavior at or near the ultimate load conditions at which debonding occurs, while investigating the influences of plate area, development length, concrete strength, and clear cover.

Instrumentation

To meet the objective of the experimental program, it was necessary to measure the extensional strain in the carbon FRP at as many points as possible along the length of the plate. Using the change in strain over each measurement interval, the shear stress could then be determined from static equilibrium, knowing that the FRP is a linear material. The strain measurement was accomplished in two ways. For the first 28 beams (25 strengthened and three controls), designated as the strain-gaged (SG) group, conventional foil resistance strain gages were used, while for the remaining five beams (four strengthened and one control), designated as the DIC group, the photographic strain analysis technique of digital image correlation (DIC) was used.

Strain-Gaged (SG) Test Group

For the SG group, 12 gages were used along each FRP plate, though in rare instances several gages were lost due to malfunctioning or debonding. The gages were bonded along the centerline of the FRP plate, as shown in Fig. 1, with closer spacing toward the plate ends. Gage lengths were typically 9.5 mm for the three gages closest to the plate ends, while 25 mm gages were used for the fourth gage from the plate end, and the remaining gages were 50-mm long.

Digital Image Correlation (DIC) Test Group

Digital image correlation (DIC) is a well-established technique for full-field strain measurement that has been used for a variety of engineering applications (Sutton et al. 1999, 2001; Verhulp et al. 2004), including the investigation of FRP that is bonded to concrete (Wan et al. 2004). For two-dimensional problems, the correspondence between the digital images, taken before and after a load is applied, is used to measure the surface strains in the test specimen. Before loading, a random, black and white speckle pattern is typically painted on the surface of the specimen and an unloaded image is taken. At each load stage, additional images

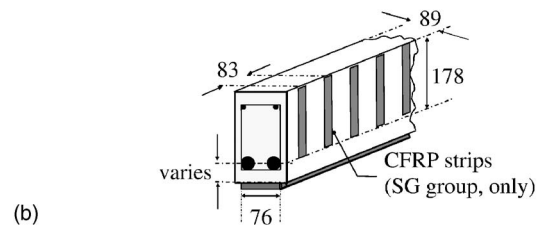
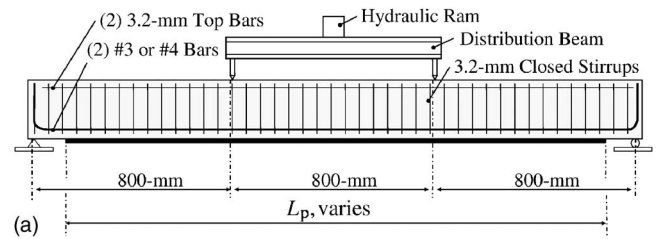


Fig. 2. Test beam and dimensions (a) side view; (b) isometric view

are acquired. Analytically, the images are divided into small subsets of gray level data. Each subset from the unloaded image is selected and mapped to the loaded image, while allowing translation, rotation, and constant strain within the subset. The gray levels for each of the pixels in the original subset are then compared with the gray levels at their mapped location in the second image using a cross-correlation error function and the parameters of the mapping function are optimized to reduce the error function to its minimum using standard Newton-Raphson-based optimization techniques. This process is repeated for all of the other subsets in the area of interest, resulting in a full-field map of the surface displacements.

Three-dimensional digital image correlation combines the surface tracking capabilities of traditional two-dimensional digital image correlation with the three-dimensional measurement capabilities of a two-camera, stereoscopic imaging system. While both the theoretical development for stereo imaging and two-dimensional image correlation are well documented, the practical application of stereovision to DIC is still a developing field. The present work uses a displacement measurement method that allows arbitrary placement of the cameras, use of standard photographic lenses, perspective correction, and a relatively simple camera calibration, based on the method developed by Helm et al. (1996).

The principal advantage that DIC offers over a series of conventional resistance gages for the strain analysis of the FRP plate is that the DIC displacement measurement is continuous over the entire plate width and length, while strain gages, providing values at single points, leave the data that is between the gages to be assumed, rather than definitively determined. In particular, the advantage DIC offers this program is continuous strain measurement that extends all the way to the plate end.

A two-camera stereoscopic DIC system was used to measure the three-dimensional displacements of the FRP plate. A 3D system was chosen over a simpler 2D system because the out-of-plane movement of the FRP plate is significant enough to warrant consideration when computing strain, and this consideration is only possible if 3D DIC is employed.

The DIC test group consisted of four strengthened beams and one control beam. The purposes of this test group were: to verify the results from the SG group, to provide a more detailed stress analysis, and to explore the use of digital image correlation for the stress analysis of reinforced concrete structures. The DIC

Table 1. SG Group Specimens and Results

Beam number ^a (1)	Clear cover (mm) (2)	Failure mode ^b (3)	Ultimate load (kN) (4)	Maximum FRP force (kN) (5)	At 95% ultimate load		
					Average shear stress ^c (MPa) (6)	Estimated peak shear stress ^d (MPa) (7)	Stress concentration factor (7)/(6)(8)
A Series: $f'_c=21$ MPa, FRP $t_p=0.330$ mm, FRP length $L_p=2,235$ mm							
2	3	D	46.76	61.68	1.13	1.22	
3	6	C	48.33	61.91	1.13	1.02	
4	19	C	50.46	57.72	1.06	1.07	
<i>Beam Series A average:</i>					1.08	1.10	1.0
B Series: $f'_c=21$ MPa, FRP $t_p=0.330$ mm, FRP length $L_p=1,730$ mm							
6	3	C	41.52	46.48	1.31	1.16	
7	6	D	44.62	49.98	1.41	1.17	
8	38	D	47.52	39.14	1.10	1.43	
<i>Beam Series B average:</i>					1.28	1.25	1.0
C Series: $f'_c=21$ MPa, FRP $t_p=0.660$ mm, FRP length $L_p=2,235$ mm							
9	3	C	54.64	92.58	1.69	2.36	
10	6	D	54.39	89.41	1.64	2.10	
<i>Beam Series C average:</i>					1.66	2.23	1.3
D Series: $f'_c=21$ MPa, FRP $t_p=0.660$ mm, FRP length $L_p=1,730$ mm							
11	3	D	48.23	58.13	1.64	2.76	
12	6	D	40.82	54.17	1.53	2.14	
13	19	D	44.09	42.23	1.19	3.22	
<i>Beam Series D average:</i>					1.45	2.71	1.9
E Series: $f'_c=41$ MPa, FRP $t_p=0.660$ mm, FRP length $L_p=1,730$ mm							
15	3	D	52.57	69.55	1.96	3.20	
16	6	D	48.75	59.39	1.68	3.63	
17	19	D	54.55	56.53	1.60	2.79	
<i>Beam Series E average:</i>					1.74	3.21	1.8
F Series: $f'_c=55$ MPa, FRP $t_p=0.330$ mm, FRP length $L_p=2,235$ mm							
19	3	C	66.69	52.09	0.95	1.37	
20	3	D	71.15	57.39	1.05	0.96	
21	6	C	69.23	59.62	1.09	1.17	
22	19	D	77.99	72.71	1.33	1.18	
<i>Beam Series F average:</i>					1.11	1.17	1.1
G Series: $f'_c=55$ MPa, FRP $t_p=0.330$ mm, FRP length $L_p=1,730$ mm							
23	3	C	66.68	53.69	1.52	2.49	
24	6	D	72.51	53.78	1.52	1.57	
25	19	C	74.33	57.40	1.62	1.55	
<i>Beam Series G average:</i>					1.55	1.87	1.2
H Series: $f'_c=55$ MPa, FRP $t_p=0.660$ mm, FRP length $L_p=1,220$ mm							
26	6	D	57.83	27.97	1.56	1.99	1.3
I Series: $f'_c=55$ MPa, FRP $t_p=0.660$ mm, FRP length $L_p=2,235$ mm							
27	19	D	83.08	79.09	1.45	1.47	1.0
28	38	D	90.59	83.30	1.52	1.64	
<i>Beam Series G average:</i>					1.49	1.56	1.0

^aControl beams are omitted from this list: Beam 1 (for Series A, B, C, D), Beam 14 (for Series E), and Beam 18 (for Series F, G, H, I) with ultimate loads of 26.72, 35.43, and 52.28 kN, respectively.

^bC denotes a compressive failure; D denotes a debonding failure.

^cObtained by dividing the maximum FRP force by the plate area in the shear span.

^dEstimated by averaging the peak values measured at the two plate ends.

group control was constructed to the same specifications as the SG group control Beam 1, while the remaining beams were two pairs of tests, modeled after SG group Beams 10 and 12. Beams 10-DIC-1 and 10-DIC-2 were both modeled after Beam 10, with instrumentation being the only distinction between the tests. Beam 10-DIC-1 used a single two-camera 3D DIC setup to measure displacement over approximately 1,500 mm of beam length with the intention of providing broad strain measurement over the middle portion of the plate length. In contrast, Beam 10-DIC-2 used two 3D DIC camera setups to focus on strain measurement near the plate ends, one camera setup covering an 800 mm length along one shear span, while the other camera setup focused exclusively along a distance of about 200 mm from the plate end. Beams 12-DIC-1 and 12-DIC-2 were similar.

While DIC displacement measurement is continuous, the process of computing strains remains analogous to conventional strain gages. In order to compute strains with DIC, one must decide the distance over which the change in lengths will be computed, a kind of "gage length." If a relatively large gage length is chosen, the total change in length will be known with very high accuracy, but output will not accurately reflect rapid changes in strain, occurring over very short distances. This is equivalent to using a very large conventional strain gage. Conversely, if a smaller gage length is chosen for the DIC strain analysis, rapid changes may be captured, but certainty is correspondingly reduced. The other decision that must be made in a DIC strain analysis is the "step size," which can be thought of as the spacing of physical gages.

For the 10-DIC-1 and 12-DIC-1 beams, covering the largest areas, the chosen gage length was 160 mm, with a step size of 4 mm. This means that a strain measurement is made every 4 mm, taken as the average strain over a 160 mm length (over the entire plate width). This process is analogous to using 375 physical gages, each 160 mm long and of the same width as the FRP, bonded on top of one another in a staggered fashion, 4 mm on center, over the complete 1,500 mm viewing area.

For the 10-DIC-2 and 12-DIC-2 beams, the longer of the two viewing areas used 80 mm gage lengths with a 3 mm step size, while the shorter view areas used 40 mm gage lengths with 2 mm step sizes.

Test Beams and Materials

The testing program consisted of 33 reinforced concrete beams, tested in four-point flexure over a simple span of 2,400 mm with loads located at one-third points [Fig. 2(a)]. All beams had widths b of 89 mm and effective depths to the tension steel d of 178 mm. The clear cover was varied as one of the studied parameters.

Internally, the tension reinforcement consisted of two standard No. 3 (9.5 mm) or No. 4 (12.7 mm) ASTM deformed grade 60 steel rebars, while the compression reinforcement consisted of two 3.2 mm diam cold-drawn smooth bars. Shear reinforcement consisted of closed stirrups, bent from the same bar stock as the compression reinforcement. The average yield stresses of the No. 3, No. 4, and 3.2 mm bars were 467.7, 455.6, and 586.1 MPa, respectively, while the average ultimate strengths were 685.3, 723.6, and 661.9 MPa, respectively.

The stirrups for the SG group were not overdesigned, i.e., the stirrup spacing of 83 mm was sufficient for the control beam to reach flexural failure, but not sufficient for the strengthened beam to reach flexural failure without also externally strengthening in shear. Consequently, 0.165 mm thick carbon FRP strips were externally bonded to the beams within the shear span at the same

spacing as the stirrups, each strip 13 mm wide by 180 mm long [Fig. 2(b)]. This was done to simulate field conditions in which it can be expected that beams requiring additional flexural strength would also require corresponding shear strengthening. The strips were intentionally made the same length as the internal stirrups so that the effect would be limited to the prevention of a panel shear failure, while not providing any confinement for the FRP flexural strengthening plate. As a verification of this, the DIC test group, identical in other respects, eliminated the FRP strips and used a stirrup spacing of 50 mm, with no resulting change in failure load or pattern.

The carbon fiber strengthening system for all of the beams was MBrace (2005), consisting of unidirectional carbon tow sheets, a low viscosity two-part epoxy primer to prepare the concrete surface, and a more viscous epoxy that is used to impregnate tow sheets and bond the composite to the concrete. However, a change in the manufacturing of the tow sheet, which occurred between the testing of the SG and DIC groups meant that the carbon tow sheet used for the DIC program had an elastic modulus of 228 GPa, while for the SG group it was 259 GPa, with both results coming from tests on the fully cured composite material. Both materials were linear elastic until the failure stress, which exceeded 3,960 MPa. In addition, dogbone tension samples of the plain saturant epoxy were cured for several weeks, strain gaged, and tested, exhibiting an overall nonlinear stress-strain behavior that was approximately linear until 40% of the ultimate stress. The elastic modulus E_a was 2.96 GPa and the Poisson's ratio of 0.43, indicating a shear modulus G_a of 1.04 GPa.

Prior to applying the FRP, the beams were meticulously prepared (Kurtz 2000). This preparation began with preloading each beam in four-point flexure to a load corresponding to 2/3 of the yield load. Following unloading, a diamond abrasive wheel was used to remove approximately 2 mm of concrete, giving full aggregate exposure. Sandblasting was used subsequently, followed by wet scrubbing with a stiff brush. Finally, beams were blown dry and cleaned with compressed air and allowed to dry thoroughly for 24 h before priming.

FRP application followed one day after priming. Conventional hand lay-up techniques, using a hard plastic roller and rubber squeegee along with firm hand pressure on the tow sheets led to a composite of very high fiber density with an adhesive thickness between the FRP and the concrete of no more than 0.5 mm, a value that was verified by saw-cutting representative samples.

Studied Parameters

Within the SG test group, four parameters were varied: The clear cover over the rebar, the FRP plate length L_p , the FRP fiber thickness (area), and the concrete cylinder strength. The DIC test group did not introduce or change any parameters. Instead, its tests were duplications of SG tests 1, 10, and 12.

The effect of clear cover was studied throughout the SG test group by varying the clear cover at four levels: 3, 6, 19, and 38 mm. Though the thickness of all clear covers used may be considered small, their values are in the correct proportions to the beam size. In addition, small coarse aggregate (9.5 mm maximum size) was used. The two smallest clear covers were attained by significant grinding of the bottom surface using a diamond abrasive wheel. In the 3 mm case, the concrete cover was ground until the shear stirrups began to be exposed, so that this clear cover was equal to the stirrup bar thickness.

With one exception (Beam 26 with $L_p=1,220$ mm), all of the

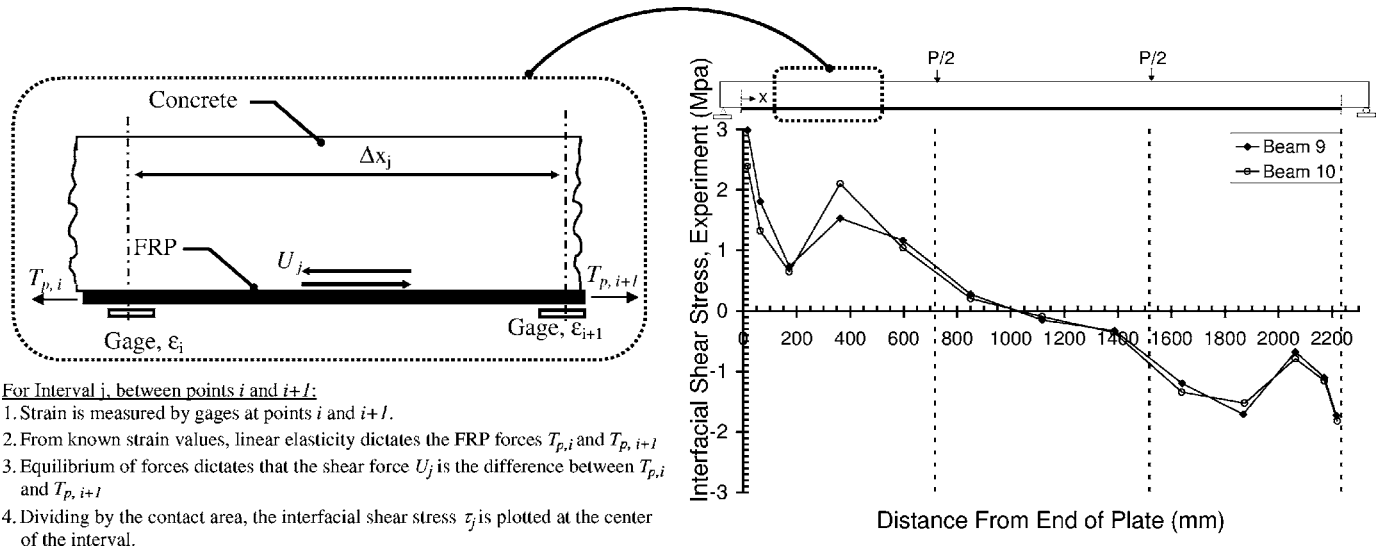


Fig. 3. Development of an interfacial shear stress plot, illustrated

strengthened beams had a plate length L_p of either 2,235 mm or 1,730 mm, giving a length L_{pd} in the shear span of either 718 mm or 465 mm.

The carbon tow sheet, with a nominal fiber thickness of 0.165 mm, was applied with either two or four layers, resulting in fiber thickness of either 0.330 mm or 0.660 mm, as shown in Table 1. The width of the FRP was 76 mm for all beams.

Concrete cylinder strength was varied at three levels: 21, 41, and 55 MPa. All concrete was laboratory mixed in small batches using a drum mixer, yielding one or two beams per batch. All beams were placed in a moist room for a minimum of 56 days to assure uniformity at the time of testing. The materials used were 9.5 mm maximum size crushed trap rock as coarse aggregate, natural sand (fineness modulus=2.8), and Type I cement, using proportions necessary to yield a 100 mm slump. For the 55 MPa mix, a small amount of high range water reducing admixture was used to keep the amount of cement used within normal limits.

Interpreting the Experiments

Interfacial Shear Stress

The interfacial shear stress is computed using static equilibrium and the recorded strain values in the same manner used by Jones et al. (1988), as illustrated in Fig. 3, using Beams 9 and 10 as examples. The figure shows a length of FRP plate that is bounded by strain gages at each end. To begin with, the shear force acting over interval j must be the difference between the plate forces at each end i and $i+1$, by static equilibrium

$$U_j = T_{p,i+1} - T_{p,i} \quad (1)$$

Because the carbon FRP is a linear elastic material, the plate forces at each end i and $i+1$ result directly from the experimentally obtained strain readings

$$T_{p,i} = A_p E_p \varepsilon_{p,i} \quad T_{p,i+1} = A_p E_p \varepsilon_{p,i+1} \quad (2)$$

Combining Eqs. (1) and (2) and dividing the shear force by the shear area of the interval, which is the product of the interval length Δx_j and b_p , leads to the average shear stress τ_j along the j th interval

$$\tau_j = \frac{E_p A_p (\varepsilon_{p,i+1} - \varepsilon_{p,i})}{b_p \Delta x_j} \quad (3)$$

Plotting the average shear stress τ_j at the interval's center leads to a plot similar to Fig. 3. Note that Beams 9 and 10, similar in all respects except for clear cover, provide plots that closely resemble one another. Both plots are reasonably symmetric about the centerline of the beam. Consequently, the subsequent plots presented in this paper represent the average of the left and right sides, for clarity and simpler comparisons with the analytical expressions from the literature.

Interpreting Partial Debonding at the Plate End

There were several beams in the SG test program for which the strain gage closest to the plate end began to measure a negative (compressive) strain value as failure approached, as also observed by Nguyen et al. (2001). The authors interpreted this localized plate compression as curvature from peeling (in some cases it was visibly evident). As illustrated in Fig. 4, these peeling re-

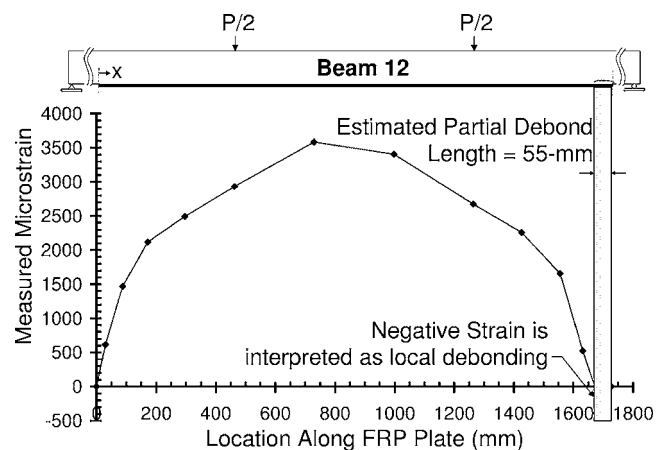


Fig. 4. Method of estimating partial debonding length

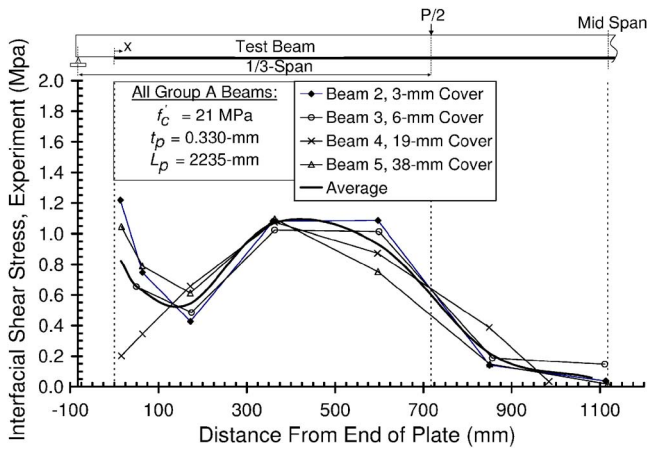


Fig. 5. Beam Series A (Beams 2, 3, 4, 5)

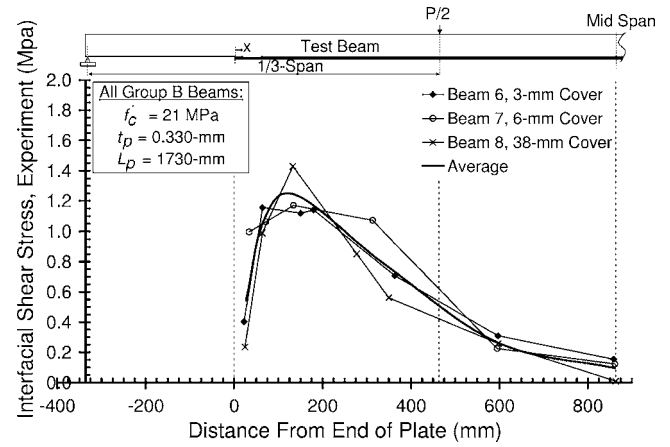


Fig. 6. Beam Series B (Beams 6, 7, 8)

gions were assumed to be debonded and the debonded length was estimated by the length of plate that was determined to have extreme-fiber compressive strain.

As described in the next section, the incidence of partial debonding led the authors to focus on the distribution of stresses, not at the ultimate condition, but at 95% of the ultimate load because, at this load level, there were only three beams (11, 12, 13) that exhibited partial debonding.

SG Group Results

All of the test beams in the SG group either failed by debonding of the FRP or by the concrete crushing in compression. However, it is quite reasonable to suggest that all of the tests represent similar conditions due to the fact that every lettered beam series had at least one debonding failure, as shown in Table 1. Hence, those beams that failed in compression differed from those that debonded only by the level of clear cover. In most cases, the difference between compression failures and debonding failures was only a 3 mm difference in clear cover. Noting also that the maximum FRP load in compression failures rarely deviates from the series average by more than a few percent, it is clear that even these beams may be considered to represent near-debonding conditions.

Similarly, the emphasis of this paper is to present the experimentally determined interfacial shear stress information that is most pertinent to the debonding problem. While it would be preferred to present these stresses at precisely the ultimate conditions, the authors found that the strain data corresponding to the ultimate conditions, immediately prior to debonding, were somewhat less consistent than the strain data at slightly lower stages of loading. Oftentimes, the ultimate load strain data showed unsymmetrical localized phenomena, such as curling or local debonding, as previously described, making the necessary process of generalization more difficult and less clear. Consequently, all of the interfacial shear stress results presented in this paper correspond to beams at 95% of their ultimate loads. This load level was chosen as a compromise level that the authors feel represents impending failure, while offering more usable results. In addition, it is felt that, as this data is used to develop predictive methods, a built-in conservatism of 5% is prudent.

Effect of Clear Cover

Of the four varied parameters, clear cover appeared to have the least influence on the behavior and distribution of interfacial shear stresses. Fig. 5 is a typical comparison of two beams, identical in all other respects except for the clear cover. The distributions of interfacial stresses are nearly identical for both beams, but Beam 9, with 3 mm clear cover exhibits slightly greater peak stresses at the plate cutoff than does Beam 10, with 6 mm clear cover. This modest trend toward sharper peak stresses was evident throughout the program, when comparing beams with 3 and 6 mm cover. Among beams with $f'_c = 21$ MPa cylinder strength (Beam Series' A, B, C, and D), the average peak shear stress at 95% of the beam's ultimate load was 1.81 MPa for beams with 3 mm cover versus 1.67 MPa for beams with 6 mm cover. Similarly, comparing 3 and 6 mm cover in beams from F and G ($f'_c = 55$ MPa), there is also a modest trend toward higher peak stresses in the beams with the smaller cover (1.61 versus 1.37 MPa). However, this trend reverses for beams with cover exceeding 6 mm, though this trend is modest, as well, compared to other factors.

The stress distribution graphs for beams that are within the same series, differing only by clear cover, are very coherent and similar to one another, as shown in Figs. 5–12. Because of the coherent nature of beams within a letter series and the relatively minor influence of clear cover on interfacial stress distribution,

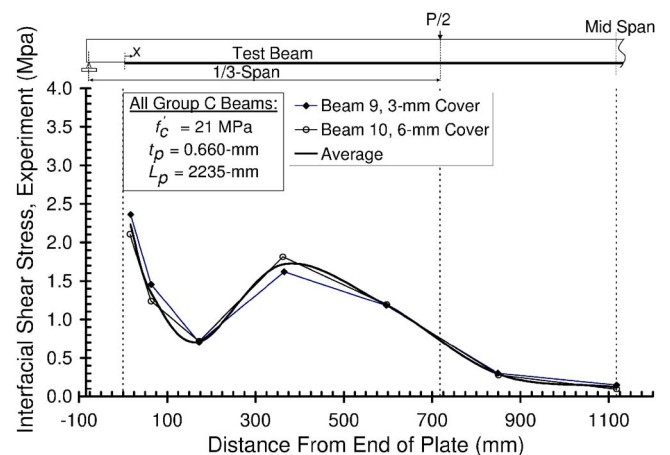


Fig. 7. Beam Series C (Beams 9, 10)

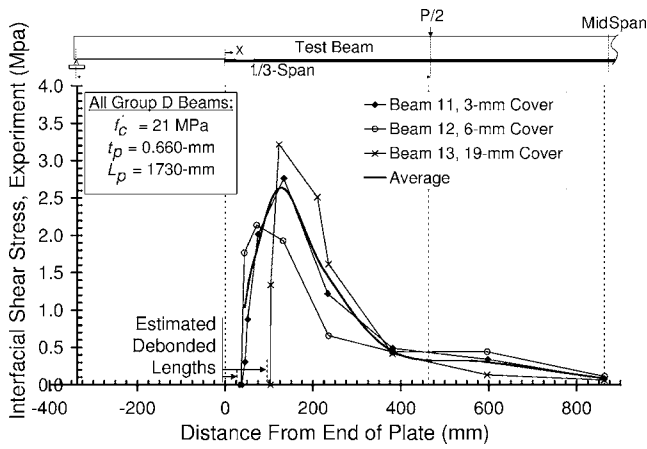


Fig. 8. Beam Series D (Beams 11, 12, 13)

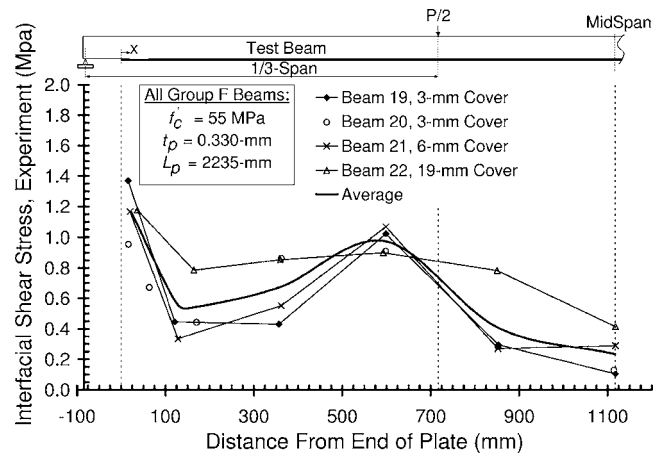


Fig. 10. Beam Series F (Beams 19, 20, 21, 22)

subsequent comparisons within this paper are based on each lettered series of tests, rather than on individual tests.

Effect of FRP Plate Length

With the exception of Beam 26, the FRP plate lengths were either 2,235 mm (corresponding to 718 mm in the shear span) or 1,730 mm (corresponding to 465 mm in the shear span). This parameter had a significant effect, not only on the overall magnitudes of stresses, but on the overall distribution of stresses, as well. Throughout the program, three sets of test series, comprising 19 tests in all, may be compared to one another to evaluate the effect of plate length: A and B, C and D, F and G.

The comparison of Series A (Fig. 5) and Series B (Fig. 6) beams reveals a marked difference. Series B Beams, with shorter plate lengths, exhibit the highest stresses near the plate cutoff, though not at the very end of the plate, as predicted by elastic analysis methods, suggesting that material softening is a factor. In contrast, the longer FRP plates of Series A Beams exhibit, not one location of peak stresses, but two. The anticipated peak occurs at the plate end, decreasing to approximately 50% of the peak level over a length of about 200 mm. The second peak, not previously anticipated or observed in the literature, is a much smoother peak that occupies the central portion of the beam's shear span. While the plate-end peak is associated with the sudden change in beam geometry, one possible explanation for the second peak is that it

is associated with the sudden application of shear at the point load. On the other hand, it is also noteworthy that the highest point of this second peak tends to correspond to the position along the span at which the rebar transitions from elastic behavior to yielding, in all of the beams in this research program.

A second centralized peak stress was not observed in the test program of Jones et al. (1988), which utilized strain-gaged plates in a similar fashion. However, in that program, relatively large external plates and internal reinforcement were used so that failure occurred without yielding, lending credence to the hypothesis that the second peak is associated with rebar yielding.

Whereas the Series A Beams display these peaks distinctly, for the Series B Beams, with shorter plate length, it appears that the two peaks have interacted to form one peak, shifted slightly from the plate end. This is important because it suggests that future research is needed to investigate the distribution of stresses on much larger beams.

The comparison of Series C (Fig. 7) with Series D (Fig. 8) and the comparison of Series F (Fig. 10) with Series G (Fig. 11) show the same changes in pattern. In all cases, there is an increase in peak stress associated with the shorter plates, but there is not generally a change in stress concentration associated with shorter plates. For the comparisons of A with B and F with G, the peak and average stresses both increase at approximately the same rate, as the plates are shortened. However, the comparison of C with D illustrates the coupled effects of larger plates with

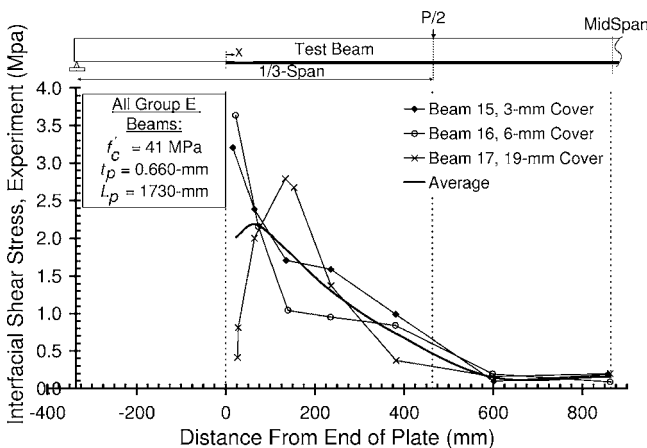


Fig. 9. Beam Series E (Beams 15, 16, 17)

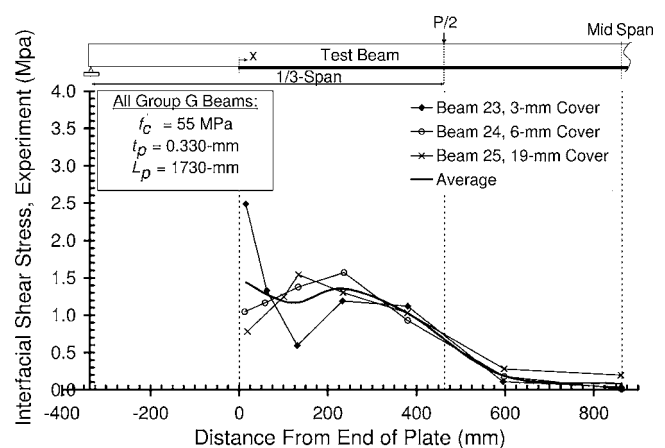


Fig. 11. Beam Series G (Beams 23, 24, 25)

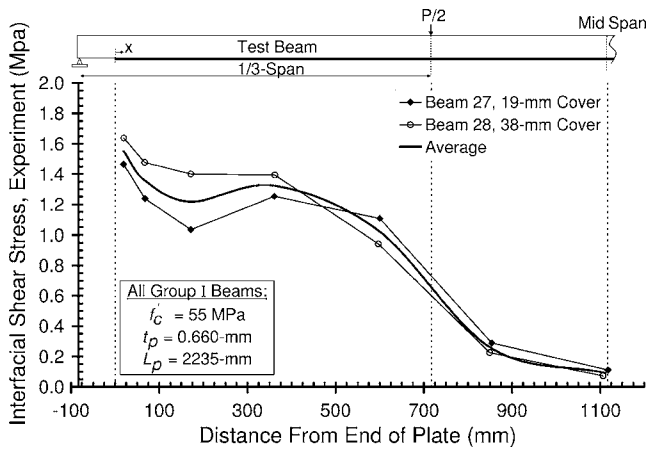


Fig. 12. Beam Series I (Beams 27, 28)

shorter development lengths on stress concentration [see column (8) in Table 1]. These beams, with thicker plates, show a dramatic increase in stress concentration, as the length of these thicker plates is shortened.

Effect of FRP Plate Area

All other factors the same, the effect of doubling the plate area may be assessed by comparing Series A (Fig. 5) to Series C (Fig. 7), Series B (Fig. 6) to Series D (Fig. 8), and Series F (Fig. 10) to Series I (Fig. 12).

For longer development lengths (A and C, F and I), doubling the plate area results in a significant increase in peak stress, a modest increase in average stress, and a modest increase in stress concentration, while not significantly changing the overall pattern of stress distribution. For shorter development lengths (B and D), the previously mentioned coupling effect is evident so that doubling the plate area results in more than a two-fold increase in peak stress, only a modest increase in average stress, and a significant increase in stress concentration.

Effect of Concrete Cylinder Strength

Ignoring the very minor differences in clear cover, the only difference between the nine beams in A, B, and C and the nine beams in F, G, and I is the concrete strength, which is 2.6 times greater in the latter case. Despite this significant difference in concrete strength between these two groups of nine beams, each group had an equal number of compression failures (four) and debonding failures (five). Furthermore, the differences in average shear stress at the ultimate

Table 2. Comparing SG and DIC Test Groups

DIC group beams			Corresponding SG beams		
Beam number	Failure mode	Failure load (kN)	Beam number	Failure mode	Failure load (kN)
1-DIC	C	25.64	1	C	26.72
10-DIC-1	D	52.16	10	D	54.39
10-DIC-2	D	53.56			
12-DIC-1	D	35.87	12	D	40.82
12-DIC-2	D	35.96			

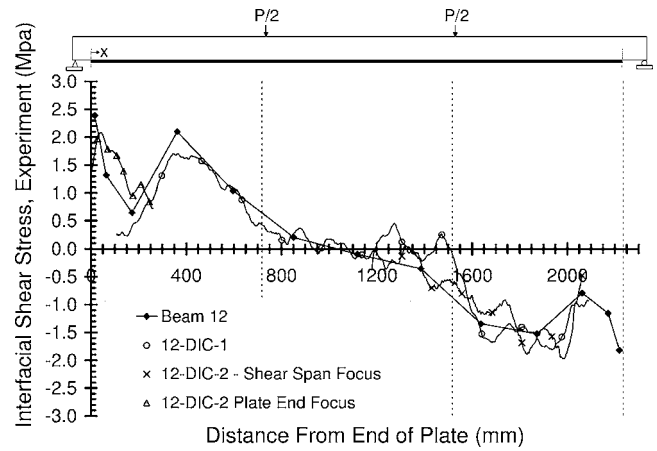


Fig. 13. Comparing Beam 12 and 12-DIC-1,2

condition among each set of nine beams were very small: 1.28 MPa ($f'_c=21$ MPa) versus 1.34 MPa ($f'_c=55$ MPa). Comparing the shear stress graphs, there does not appear to be a significant difference in stress distribution, associated with concrete strength. Concrete cylinder strength appears to have negligible influence.

DIC Group Results

The DIC group consisted of four strengthened beams and one control, modeled after SG tests 1, 10, and 12, with no substantial differences other than somewhat lower FRP elastic modulus in the DIC group. As shown in Table 2, these beams performed essentially the same as their comparison beams in the SG group, with the same failure modes and similar failure loads.

Fig. 13 illustrates that the DIC test group verifies the overall pattern of shear stress distribution found in the strain-gaged Beam 12, while also showing greater detail. While Beam 12's middle third showed linearly varying stresses in the 0 to 0.75 MPa range, the 12-DIC-1 beam shows the same magnitudes, but in the form of oscillations with a period of approximately 150 mm. The more focused strain measurement of Beam 12-DIC-2 matches the results of Beam 12, similarly. Taken together, Beams 12-DIC-1 and

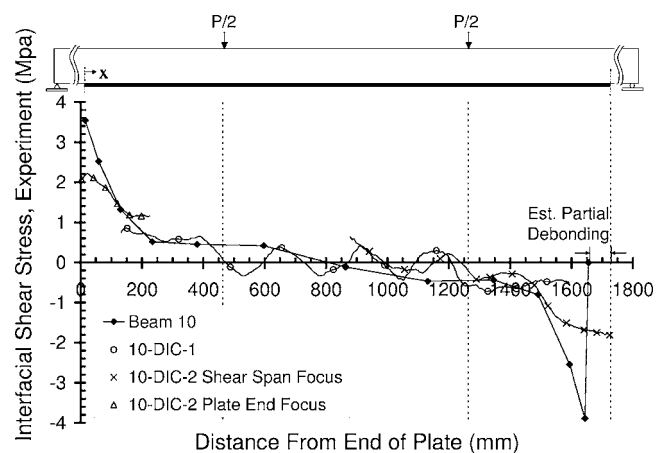


Fig. 14. Comparing Beam 10 and 10-DIC-1,2

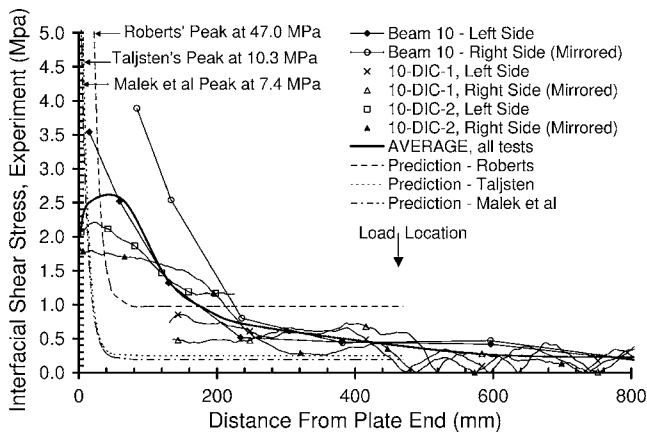


Fig. 15. Beam 10: results versus analytical predictions

12-DIC-2 show the same pattern of two peaks in each shear span, previously discussed.

Fig. 14 also illustrates the consistent patterns, measured in both the SG and DIC groups. In the middle third, the same oscillatory pattern of stress is seen, with a period of about 250 mm. The stress rise in the shear span is very similar until within 100 mm of the plate end. Near the plate end, the DIC results show smoother results, which suggests that the true behavior may involve softening of the interface, prior to debonding.

The use of DIC helps to validate the strain-gaged results, particularly near the plate ends. In the strain-gaged case, the gage closest to the plate end was a 9.5 mm gage, located 30 mm on center from the plate end, so that there was a data gap of approximately 25 mm in a crucial area. On the other hand, the DIC measurements, without any gaps, provide confirming results with the same modest concentrations in stress at the plate ends. While it is true that the DIC strain calculations were performed by integrating displacements over rather large gage lengths (40 mm at the plate end), the trends shown in Figs. 13 and 4 indicate that the shear stresses are actually dropping, approaching the plate ends. Hence, when the authors recomputed the strain using shorter gage lengths, the results showed a more pronounced decline in the stress, rather than the often-anticipated sharp peak. It is likely, then, that the plate-end peak migrates somewhat from the very end, as a consequence of material softening.

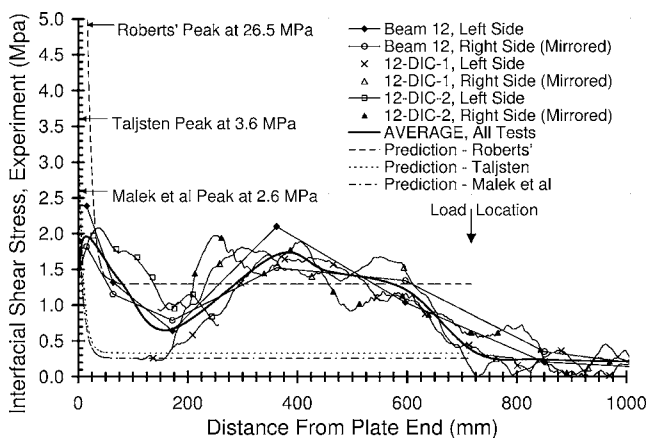


Fig. 16. Beam 12: results versus analytical predictions

Table 3. Measured versus Predicted Interfacial Shear Stresses

Beam number	Experimental results	Average shear stress at 95% of beam ultimate load (MPa)		
		Analytical predictions		
		Malek et al. (1998)	Malek et al. (1997)	Roberts et al. (1989)
5	1.02	0.12	0.14	0.97
7	1.41	0.11	0.15	0.78
10	1.64	0.26	0.33	1.30
12	1.53	0.19	0.25	0.97
20	1.05	0.11	0.15	0.56
24	1.52	0.11	0.15	0.58

Finally, it should be noted that the typical magnitudes of stress concentration at the plate ends that were observed throughout both the SG and DIC programs are similar to those observed in Jones et al. (1988), yet they are considerably less pronounced than anticipated by the analytical methods in the literature, as described in the following section.

Comparisons with Analytical Solutions

The shear stress results from Beams 10 and 12 are plotted alongside the predictive expressions of Roberts (1989), Täljsten (1997), and Malek et al. (1998) in Figs. 15 and 16, respectively. All computations needed for the three analytical expressions were based on the measured geometry and material properties reported in this paper, including the measured adhesive thickness of 0.5 mm, a value that all three expressions are highly sensitive to. For completeness, both the right and left halves of each beam are plotted, with the right half data mirrored, to show all of the available data in a compact manner. An averaged curve is presented for the clearest comparison with the three analytical expressions.

All of the plotted analytical expressions are characterized by sharp stress concentrations that begin to deviate from the steady state behavior at distances ranging from 50 to 70 mm from the plate end. Unfortunately, the relatively large gage lengths employed for the experimental measurements prohibit any comparisons within approximately 32 mm of the plate end, corresponding to the position of the first strain gage. However, Fig. 15 illustrates that the overall character of the stress distribution is altogether different from the analytical expressions over the entire shear span. In particular, the stresses begin to rise to the peak value at 150 to 250 mm from the plate end in a far more gradual manner than predicted. In addition, Fig. 16 illustrates that the actual beams show a consistent pattern of a second peak that is of nearly the same magnitude as the plate-end peak, a pattern that is not anticipated by the analytical expressions.

Though none of the analytical expressions resemble the experimental curves, the steady state response predicted by Roberts is a fair representation of the average shear stress. As Table 3 shows, the Roberts expression is typically found to be the best of the analytical models for predicting the average stress, though it always underpredicts and tends to yield a very wide range of values, so that its predictions ranged from 38 to 95% of the corresponding experimental values.

Conclusions

In the writers' opinion, the results presented in this paper provide much needed experimental information on interfacial stress distributions for reinforced concrete beams strengthened with FRP plates. The following conclusions can be drawn regarding the influence of: magnitude of clear cover, plate development length, plate thickness, and compressive strength of concrete:

- Plate lengths have significant influence on the distribution of interfacial shear stress. Shorter plates exhibited the anticipated single peak stress at the plate end. Longer plates exhibited two peaks, one associated with the plate cutoff and the other at the center of the shear span, possibly associated with the transition from elastic behavior to yielding of the internal rebar. To the best of the authors' knowledge, the second peak has not been reported in the literature. Existence of this peak will play a major role in analysis and design. For example, providing mechanical or other types of anchors at the end of the plates may not be an effective approach.
- Shortening of the plate length, by itself, results in a proportional increase in both the peak and average shear stress, hence no change in stress concentration. However, the combination of shorter and thicker plates leads to an increase in stress concentration.
- All other factors being equal, doubling the plate thickness corresponds to a 10 to 50% increase in average shear stress at the ultimate condition.
- Changes in the magnitude of clear cover do not profoundly affect the magnitudes and distributions of interfacial shear stresses, though beams with extremely small clear cover (3 mm) do tend to exhibit moderately sharper stress distributions with greater peak stresses at the plate end.
- The compressive strength of the concrete does not affect the magnitude or the distribution of interfacial shear stresses significantly.

The use of digital image correlation confirmed the findings and overall patterns that were discovered using conventional strain gages, while offering greater resolution and complete coverage of the FRP plate. Considering the DIC and SG groups together, it was found that:

- The DIC technique confirms the existence of the second peak. In addition, it was found that the second peak was higher than the plate-end peak, in many cases.
- Though the experimental methods did not enable comment on the interfacial stresses to the very end of the plate, it was found that the plate end stress begins to rise much more gradually from the steady-state stress over a larger distance than predicted by the analytical expressions of Roberts, Täljsten, and Malek et al., but consistent with the previous experimental work of Jones et al. (1988).
- None of the analytical expressions predicted the second peak in shear stress and no single expression expressed the peak and average (steady-state) stresses very well. However, the expressions of Täljsten and Malek et al. tended to predict the plate end stress relatively well, while the expression of Roberts was better able to predict the average interfacial shear stress.
- It may not be unreasonable to consider the distribution of interfacial shear stress to be uniform, as suggested by Mukhopadhyaya and Swamy (2001).

As suggested by Mukhopadhyaya and Swamy (2001) and carried further by Colotti et al. (2004), the problem of analyzing and predicting debonding failure has focused on the hypothesis

that failure is initiated as a consequence of stress concentration at the plate end. Among the difficulties with this approach is the fact that the magnitudes of plate end stresses had not, to this point, been identified experimentally. The other substantial problem has been the tendency for the analytical predictions to offer an unacceptably wide scatter of predicted end stresses, therefore, acting as poor predictors of failure. This research has contributed substantially to solving these problems. The presence of stress concentration at the plate end has been verified, but there is evidence that the concentration is less severe than predicted from elastic assumptions. In fact, it appears that the most realistic predictor of stress distribution is to assume it to be uniform, as previously suggested by Mukhopadhyaya and Swamy.

Notation

The following symbols are used in this paper:

- A_p = fiber area of FRP plate, mm²;
- b_p = width of the FRP plate, mm;
- DIC = digital image correlation; refers to the test beams that used digital image correlation;
- E_a = modulus of elasticity of the epoxy adhesive, GPa;
- E_p = modulus of elasticity of FRP plate, based on the fiber area, GPa;
- FRP = fiber-reinforced polymer;
- f_y = yield strength of steel, MPa;
- f'_c = 28-day cylinder strength of concrete, MPa;
- G_a = shear modulus of the epoxy adhesive, GPa;
- L_p = the overall length of the FRP plate, mm;
- SG = strain gaged; refers to the strain-gaged test beams;
- $T_{p,i}$ = plate force at gage i ;
- U_j = shear force between concrete and the FRP plate, on interval j ;
- x = distance measured from the end of the FRP plate, mm;
- ϵ_p = FRP plate strain; and
- τ_j = interfacial shear stress between FRP plate and concrete on interval j , MPa.

References

- Arduini, M., and Di Leo, A. (1996). "Composite behavior of partially plated beams in the linear range." *Repair and strengthening of concrete members with adhesive bonded plates*, ACI No. SP-165, R. N. Swamy and R. Gaul, eds., American Concrete Institute, Detroit, 43–53.
- Colotti, V., Spadea, G., and Swamy, R. N. (2004). "Structural model to predict the failure behavior of plated reinforced concrete beams." *J. Compos. Constr.*, 8(2), 104–122.
- Helm, J. D., McNeill, S. R., and Sutton, M. A. (1996). "Improved three dimensional image correlation for surface displacement measurement." *Opt. Eng.*, 35(7), 1911–1920.
- Jones, R., Swamy, R. N., and Charif, A. (1988). "Plate separation and anchorage of reinforced concrete beams strengthened by epoxy-bonded steel plates." *Struct. Eng.*, 66(5), 85–94.
- Kurtz, S. (2000). "Failure criteria for reinforced concrete beams strengthened with carbon composites." Ph.D. thesis, Rutgers Univ., Piscataway, N.J.
- Malek, A. M., Saadatmanesh, H., and Ehsani, M. R. (1998). "Prediction of failure load of R/C beams strengthened with FRP plate due to stress concentration at the plate end." *ACI Struct. J.*, 95(2), 142–152.
- MBrace. (2005). (www.mbrace.com).

- Mukhopadhyaya, P., and Swamy, N. (2001). "Interface shear stress: A new design criterion for plate debonding." *J. Compos. Constr.*, 5(1), 35–43.
- Nguyen, D. M., Chan, T. K., and Cheong, H. K. (2001). "Brittle failure and bond development length of CFRP-concrete beams." *J. Compos. Constr.*, 5(1), 12–17.
- Oehlers, D. J. (1992). "Reinforced concrete beams with plates glued to their soffits." *J. Struct. Eng.*, 118(8), 2023–2038.
- Quantrill, R. J., Hollaway, L. C., and Thorne, A. M. (1996). "Predictions of the maximum plate end stresses of FRP strengthened beams: Part II." *Mag. Concrete Res.*, 48(177), 343–351.
- Ritchie, P. A., Thomas, D. A., Lu, L. W., and Connelly, G. M. (1991). "External reinforcement of concrete beams using fiber-reinforced plastics." *ACI Struct. J.*, 88(4), 490–500.
- Roberts, T. M. (1989). "Approximate analysis of shear and normal stress concentrations in the adhesive layer of plated RC beams." *Struct. Eng.*, 67(12), 229–233.
- Roberts, T. M., and Haji-Kazemi, H. (1989). "Theoretical study of the behaviour of reinforced concrete beams strengthened by externally bonded steel plates." *Proc. Inst. Civ. Eng., Part 2. Res. Theory*, 87, 39–55.
- Saadatmanesh, H., and Ehsani, M. R. (1991). "RC beams strengthened with GFRP plates. I: Experimental study." *J. Struct. Eng.*, 117(11), 3417–3433.
- Sharif, A., Al-Sulaimani, G. J., Basunbul, I. A., Baluch, M. H., and Ghaleb, B. N. (1994). "Strengthening of initially loaded reinforced concrete beams using FRP plates." *ACI Struct. J.*, 91(2), 160–168.
- Shen, H.-S., Teng, J. G., and Yang, J. (2001). "Interfacial stresses in beams and slabs bonded with thin plate." *J. Eng. Mech.*, 127(4), 399–406.
- Spadea, G., Bencardino, F., and Swamy, R. N. (1998). "Structural behavior of composite RC beams with externally bonded CFRP." *J. Compos. Constr.*, 2(3), 132–137.
- Sutton, M. A., Helm, J. D., and Boone, M. L. (2001). "Experimental study of crack growth in thin sheet 2024-T3 aluminum under tension-torsion loading." *Int. J. Fract.*, 109(3), 285–301.
- Sutton, M. A., McNeill, S. R., Helm, J. D., and Chao, Y. J. (1999). "Advances in two-dimensional and three-dimensional computer vision methods for the measurement of surface shape and surface deformations on simple and complex objects." *Photomechanics for Engineers*, Pramod Rastogi, ed., Springer-Verlag, New York, 323–372.
- Täljsten, B. (1997). "Strengthening of beams by plate bonding." *J. Mater. Civ. Eng.*, 9(4), 206–212.
- Verhulp, E., van Rietbergen, B., and Huiskes, R. (2004). "A three-dimensional digital image correlation technique for strain measurements in microstructures." *J. Biomech.*, 37(12), 1313–1320.
- Wan, B., Sutton, M. A., Petrou, M. F., Harries, K. A., and Li, N. (2004). "Investigation of bond between fiber-reinforced polymer and concrete undergoing global mixed mode I/II loading." *J. Eng. Mech.*, 130(12), 1467–1475.